

Highlights

Neutron Yield Predictions with Artificial Neural Networks: A Predictive Modeling Approach

Benedikt Schmitz, Stefan Scheuren

- Fast inference model to predict neutron yields.
- Model reproduces experimental data.
- Model can compare between arbitrary ion sources.
- Yield predictions can be adjusted and improved with each new data set.
- Model and data are openly available.

Neutron Yield Predictions with Artificial Neural Networks: A Predictive Modeling Approach

Benedikt Schmitz^a, Stefan Scheuren^b

^a*Technische Universität Darmstadt
Institut für Teilchenbeschleunigung und Elektromagnetische Felder
(TEMF), Schlossgartenstr. 8, Darmstadt, 64289, Germany*

^b*Technische Universität Darmstadt
Institut für Kernphysik (IKP), Schlossgartenstr. 9, Darmstadt, 64289, Germany*

Abstract

The development of compact neutron sources for applications is extensive and features many approaches. Let alone ion-based approaches, several projects with different parameters exist. This article focuses on ion-based neutron production below the spallation barrier for arbitrary light ion beams. With this model, it is possible to compare different ion-based neutron source concepts against each other quickly. This contribution derives a predictive model using Monte Carlo simulations (50k simulations) and deep neural networks. This model can skip the necessary Monte Carlo simulations, which individually take a long time to complete, increasing the effort for optimization and predictions. The models' shortcomings are addressed, and mitigation strategies are proposed.

Keywords: Neutron, Thick Target Yield, Artificial Neural Network, Modelling, Monte Carlo, bootstrapping

1. Introduction

The European Spallation Source ESS, the world's brightest neutron source, is nearing completion and further concentrates research with neutrons to only a few powerful facilities. This concentration is increased by the successive shutdown of European research reactors and counteracted by the development of compact sources at several institutions [1, 2, 3]. The loss of these sources further causes a decline in the available beam time as displayed in Figure 1. Compact neutron sources can also counteract this since several can be commissioned and used at the institutes where they are needed.

1.1. Physical constraints

These different concepts under development have in common that they use light ion projectiles (protons or deuterons) on a low mass target

(e.g., lithium, beryllium[1], tantalum[2]) and have particle energies below the spallation threshold (< 100 MeV [5, pp. 1008 f]. Accelerator-based neutron sources are scalable, and for low-energy particles below the spallation threshold, nuclear waste is less of an issue, leaving compactness as the remaining issue. Compact accelerators generally mean that only lower energies can be achieved, which causes a reduction in the neutron yield. This makes a trade-off necessary for conventional accelerators since the accelerator can not become genuinely compact if high energies should be achieved, which increases the final neutron yield. The different approaches, also mentioned in this article, are based on projectile energies lower than 100 MeV [6, 7, 2, 1, 3]. Furthermore, higher neutron energies allow us to penetrate thicker materials and increase the number of applications for this source type, for example, in homeland security applications [8].

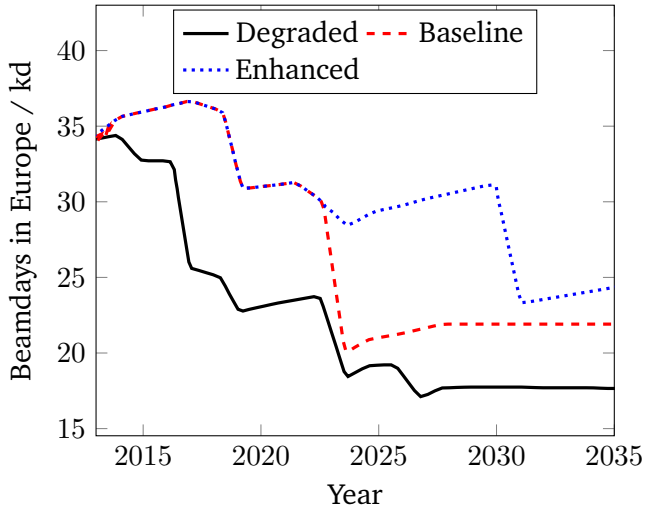


Figure 1: Prediction of the available beam days for neutron radiation in Europe. Three potential scenarios are displayed. Its differences are caused by the assumption of different remaining runtimes from existing machines and different commissions of new instruments, especially at the ESS. Enhanced includes faster commissioning of the ESS instruments and longer runtime, while Degraded assumes a faster decommissioning and delay in the Ess commissioning. The detailed explanation for each scenario is given in the ESFRI’s report [4, pp. 66-77].

Models that ensure comparability along these different concepts and are quick to evaluate are essential for developing, comparing, and improving compact neutron sources. Models and results created by the individual institutions for their systems are not necessarily comparable since different nuclear cross-section libraries and measurement methods are used.

Furthermore, our approach for a compact neutron source uses a laser-driven ion acceleration via the Target Normal Sheath Acceleration mechanism (TNSA)[6]. TNSA ejects an exponential energy spectrum, which starkly contrasts the mono-energetic particles created by conventional accelerators.

1.2. Outline

In this work, we will present a model capable of evaluating a neutron source setup quickly and precisely in the relevant energy area and for arbitrary input bunches.

Data-driven modeling needs a large dataset of consistent experimental data distributed over the

parameter range of interest. Due to the nonexistence of such a data set in the relevant energy range, simulations were used as the basis for modeling. The few data sets measured with similar parameters are used as test cases later in this work.

The simulation results are used to devise a surrogate model based on artificial neural networks to predict the double differential neutron yield dynamically. For the uncertainty prediction, bootstrap training for the model was done.

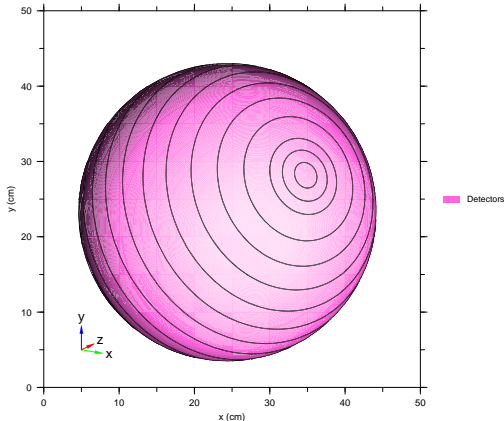
2. Methods

2.1. Simulations

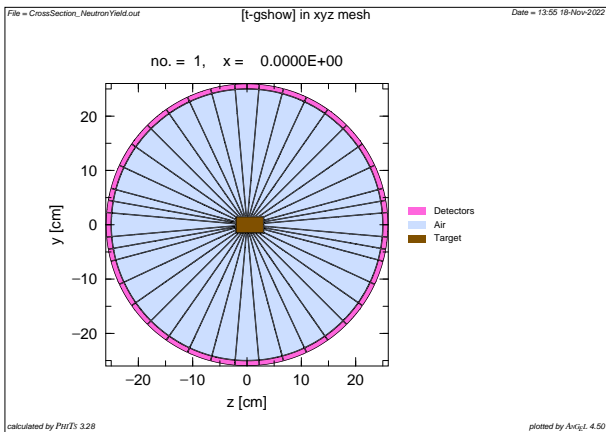
We simulated the neutron yield with Monte Carlo Simulations utilizing the PHITS [9] code in Version 3.28A with the FENDL [10] library in Version 3.

The observable is the double differential neutron yield \mathfrak{F} which is determined by measuring the number of neutrons crossing a detector surface. We implemented several detectors as rings around the converter to resolve the scattering angle. This is illustrated in 2a and 2b, where the black lines indicate the boundaries for each detector. We give the concrete parameters for the scattering angle (center of the detector) Θ and its size $\Delta\Theta$ in the Appendix Appendix A in table A.4.

The cylindrical particle beam is inserted at position $(0, 0, -9)$ into positive z direction with a radius of $r_0 = 0.5$ cm. Energy and particle type of the incoming particles are subject to variation as indicated by Table 1. The target is implemented as a cylinder along the z -axis centered around $(0, 0, 0)$ with a radius $r = 1.5$ cm and a variable length as well as a variable material, as indicated by Table 1, too. We ensured that target was long enough to stop the full bunch inside the target. It is possible, however, that the target is longer than necessary to include low neutron absorption and moderation. This is important since non-mono energetic beams are to be investigated; this would otherwise yield an overestimation of the neutron yield at higher energies. The target cylinder’s radius was fixed at 2.5 cm. We acquired



(a) 3D view of the simulation setup used in the PHITS simulations.



(b) 2D Cross section of the simulation geometry.

Figure 2: Simulation description plots. They are created using PHITS Angel tool.

Table 1: Monte Carlo input parameters. The maximum number of sampled parameters is given in the last column. Rectangular brackets indicate numerical intervals with the lower value left and the upper value right inside the bracket.

Quantity	Values	Steps
Projectile	Deuterons, Protons	2
$E_{\text{kin}} / \text{MeV}$	[3, 97]	56
Element	Li, LiF, Be, Va, Ta	5
Length / mm	[0.02, 104.45]	356
Angle / °	[0, 180]	21

a total of 54 768 neutron yield simulations in the mentioned setup.

Data preparation

We organized the data as follows: We labeled the categorical data features according to a binary representation of the values, while the continuous data was scaled from 0 to 1. The two different projectiles can then be labeled by a single bit: Deuterium is labeled with 1, and Hydrogen is labeled with 0. For the converter materials under investigation, this makes it necessary to have 3 bits to describe all possibilities fully: 'Li'-'000', 'LiF'-'001', 'Be'-'010', 'Va'-'011', 'Ta'-'100'

Without preparation, the model training does not converge. The data was first resampled to increase the density of the data points in the higher energy part of the spectrum, which was logarithmically sampled from the code. This resampling was done with cubic spline interpolation of the Monte Carlo output data and joined with the raw data, doubling the number of data points for learning while keeping the spectral shape intact.

Numerical stability is an issue because of the extensive range of input data, varying by several orders of magnitude. While some data points contribute much to the mean squared error training quantity, some with a lower numerical value did not contribute much. As a result, the training process was volatile, which needed to be mitigated. We fixed this by rescaling the data using the relations given in Equation 1.

$$\begin{aligned} \bar{Y} &= \log_{10}(Y) \\ \hat{Y} &= \bar{Y} / \min(\bar{Y}) \end{aligned} \quad (1)$$

where \hat{Y} is the renormalized and Y the raw data. Not at this point, the output data of the simulation is normalized to the incident particle, with the condition that the energy is below the spallation threshold, all values are smaller than 1, such that the value of the logarithm is negative. The final data reached from 1 to the normalized maximal value, and all data was larger than 0. The neutron's energy was also normalized by the cut-off energy to scale from 0 to 1.

2.2. ANN setup

We trained two models, one for the spectrum and one for the cut-off energy. Training cut-off positions together with the spectrum are difficult since a cut-off represents a discontinuity in the spectrum. Discontinuities are not smooth and can only be approximated with an even more extensive data set. The spectral shape is then normalized from minimal data at 0 to maximal non-zero data at 1, while the cut-off model predicts the relevant scaling for the predicted spectrum.

The networks are both fully connected feed-forward networks. For the spectrum, the node structure is as follows, where x_s is an 8-dimensional input vector: ($x_s \rightarrow 200 \rightarrow 200 \rightarrow 200 \rightarrow 200 \rightarrow 200 \rightarrow 200 \rightarrow 200 \rightarrow 1$). For the cutoff energy of the spectrum, the node structure is as follows, where x_c is a 7-dimensional input vector: ($x_c \rightarrow 260 \rightarrow 180 \rightarrow 180 \rightarrow 340 \rightarrow 180 \rightarrow 180 \rightarrow 340 \rightarrow 340 \rightarrow 180 \rightarrow 1$). Since the spectrum model yields a full spectrum, an additional parameter marking the position inside the spectrum must also be used.

Better results might be acquired by dropout optimization or other sophisticated methods, but time constraints did not permit further optimizing the topology. The selected hyperparameters are given in Appendix B

2.3. ANN bootstrap

The simulation data has, due to its probabilistic nature, an uncertainty. This uncertainty is up to 100% for some of the energy bins and cannot be taken into account directly. We circumvented this with a bootstrap method[11, 12]. The raw data was randomly resampled in the range of uncertainty. We assumed a Gaussian distribution because the code also assumed it, yielding the uncertainty in a 1σ interval. Then with this distribution function, we can resample the yield data N times:

$$Y_{\text{res}} = \mathbf{G}(\mu = Y, \sigma = \sigma_Y), \quad (2)$$

where \mathbf{G} is the Normal distribution. Applying the same procedure on each resampled spectrum yields $N + 1$ different predictions, which deviate

around the joined mean. For each set of input parameters, $N + 1$ predictions are generated. The mean of these predictions is then the predicted value, while the standard deviation of those predictions is then the uncertainty of the prediction.

2.4. Ensuring generality

The formal application of the resulting surrogate $\hat{\mathfrak{F}}$ is given by

$$\frac{d^2Y}{d\Theta dE_n} = \sum_{E_p} N_p(E_p) \cdot \hat{\mathfrak{F}}(E_n, \Theta, E_p) \Delta E_p \quad (3)$$

and with the infinitesimal limit for $\Delta E_p \rightarrow 0$:

$$= \int N_p(E_p) \cdot \hat{\mathfrak{F}}(E_n, \Theta, E_p) dE_p, \quad (4)$$

where Y is the neutron yield, Θ the scattering angle, E_n the energy of the neutron, N_p the number of incoming projectiles, E_p the energy of the projectile, and $\hat{\mathfrak{F}}$ is the unit surrogate model, which is normalized to one projectile particle. E_p is sampled according to the needed precision. We used a bin width of $\Delta E_p = 1$ MeV. Setting the model up like this enables us to apply and verify this model on mono-energetic spectra and laser-accelerated ions. This model ensures direct comparability between conventional accelerator-driven ion sources and laser-driven ion sources.

3. Results

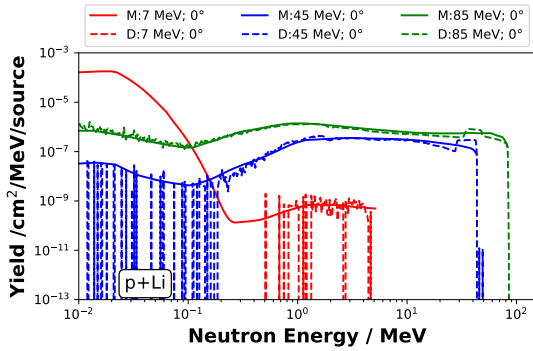
The training of all networks converged when the learning rate was consequently reduced. For each network, we extracted the mean squared error value and the normalization factor used during preprocessing and displayed them in Table 2

3.1. Validation against the Raw Simulation Data

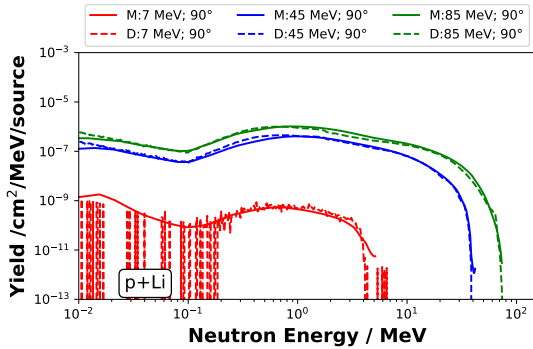
To check the validity of the surrogate, we first compare its predictions with the raw data used for training. The results are displayed in Figure 3, Figure 4, Figure 5, and Figure 6. Displayed are the full spectra created by the Monte Carlo code vs the result created by our model, with its corresponding uncertainty. We can derive a few remarks on the model's validity from these figures.

Table 2: Network metrics for all trained networks. Id 0 means the raw data is used. The other nine numbers indicate the nine resampled datasets. MSE is the mean squared error training metric, and Normalization indicates the normalization constant applied to each data set after the logarithm was applied.

Id	MSE	Normalization
0	0.00128	-16.0505
1	0.00124	-16.2796
2	0.00128	-15.9784
3	0.00119	-16.6231
4	0.00114	-16.9578
5	0.00114	-16.8753
6	0.00125	-16.1653
7	0.00120	-16.5274
8	0.00140	-15.3819
9	0.00121	-16.4534

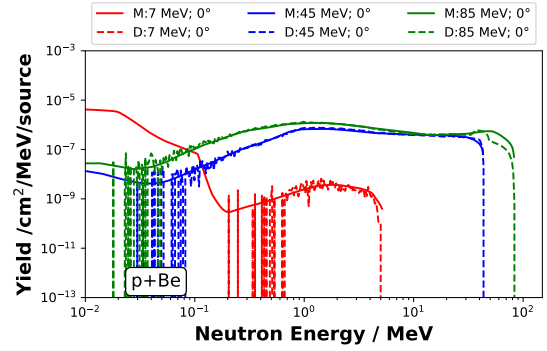


(a) (p, Li) reaction under 0° .

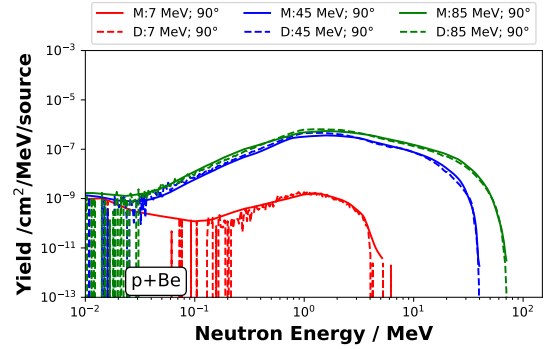


(b) (p, Li) reaction under 90° .

Figure 3: Comparison of our model with results from PHITS. Displayed are samples for proton-induced neutron production on lithium. Dashed lines indicate the Monte Carlo data indicated by D, and solid lines indicate the corresponding model output by M. The shaded area is the model's uncertainty.

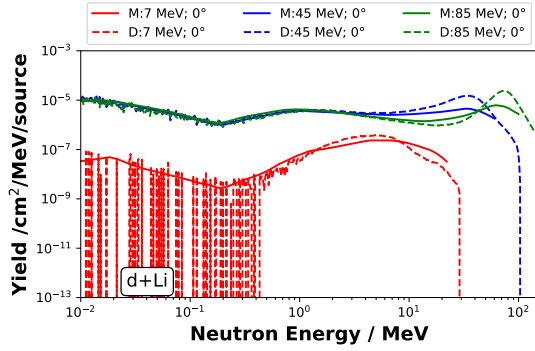


(a) (p, Be) reaction under 0° .

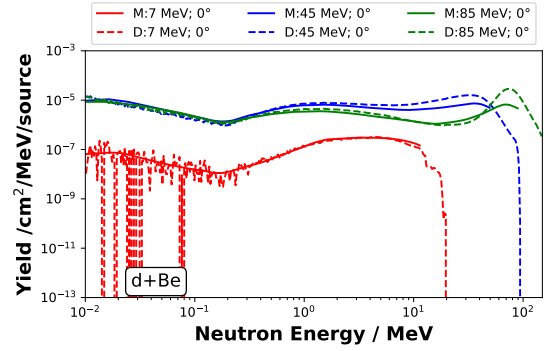


(b) (p, Be) reaction under 90° .

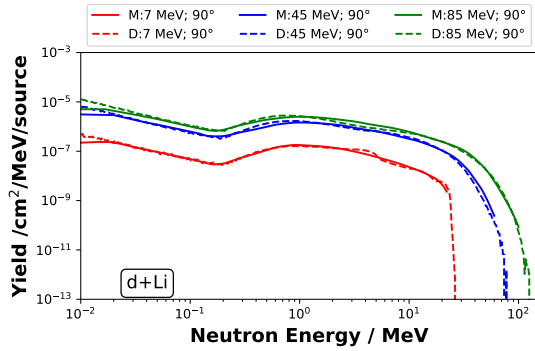
Figure 4: Comparison of our model with results from PHITS. Displayed are samples for proton-induced neutron production on beryllium. Dashed lines indicate the Monte Carlo data indicated by D, and solid lines indicate the corresponding model output by M. The shaded area is the model's uncertainty.



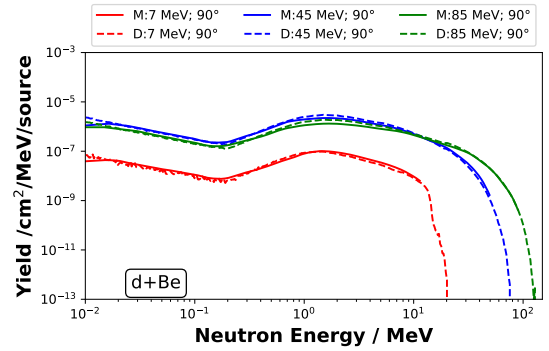
(a) (d,Li) reaction under 0° .



(a) (d,Be) reaction under 0° .



(b) (d,Li) reaction under 90° .



(b) (d,Be) reaction under 90° .

Figure 5: Comparison of our model with results from PHITS. Displayed are samples for deuterium-induced neutron production on lithium. Dashed lines indicate the Monte Carlo data indicated by D, and solid lines indicate the corresponding model output by M. The shaded area is the model's uncertainty.

Figure 6: Comparison of our model with results from PHITS. Displayed are samples for deuterium-induced neutron production on beryllium. Dashed lines indicate the Monte Carlo data indicated by D, and solid lines indicate the corresponding model output by M. The shaded area is the model's uncertainty.

1. The model is only valid in the region of fit, defined by the parameters in Table 1.
2. After the cutoff energy, the spectrum generally deviates, implying that the spectral model does not learn the physical cutoff and therefore yields wrong results in the high-energy end of the spectrum.
3. The model can predict the lowest energy neutrons, which can not be seen in the Monte Carlo spectra. These values, however, have to be used with care: Their uncertainty is very high, up to 100 %, and the result does not reproduce measurement data correctly (confer to subsection 3.2). This has two reasons: First, the model itself is regression-based, and as can be seen, higher energy projectile energies do have neutron signals in the low energy regime. The effect of the regression is calculating a corresponding mean value from all calculated spectra, yielding a non-zero contribution. Second, the reason for zero count rates is the bulky target, the lowest neutrons created by low-energy projectiles can not leave the target and are stuck there. The count rates in the Simulation are low, meaning the statistical uncertainties are high.
4. The proton lithium reaction has a characteristic high energy peak in the forward direction. This peak is suppressed by the bulky target, as seen in 3a. Due to the nature of the regression model, the model further suppresses the peak and is, therefore, impossible to resolve.
5. The cutoff energies mean squared error is approximately 9 MeV^2 . This implies an uncertainty of the cut-off energy of approximately $\pm 3 \text{ MeV}$.

Despite these limitations, the model can predict accurate spectra over a large energy domain in milliseconds evaluation time and allows quick evaluations of neutron production.

3.2. Validation against Experimental Data

The largest experimental data collection is the EXFOR database, hosted by the International Atomic Energy Agency (IAEA)[13, 14]. Only a few data

Table 3: Parameters for several compact neutron source accelerators. The same projectile and target types are fixed as protons and beryllium to compare different spectra. The sources are given in the text.

Name	Energy	Current	d_T
Unit	MeV	10^{-4} A	mm
IAEA2	40	50	20
IAEA4	40	1250	20
RANS	7	1	0.3
HBS	70	1000	16
SONATE	20	1000	2

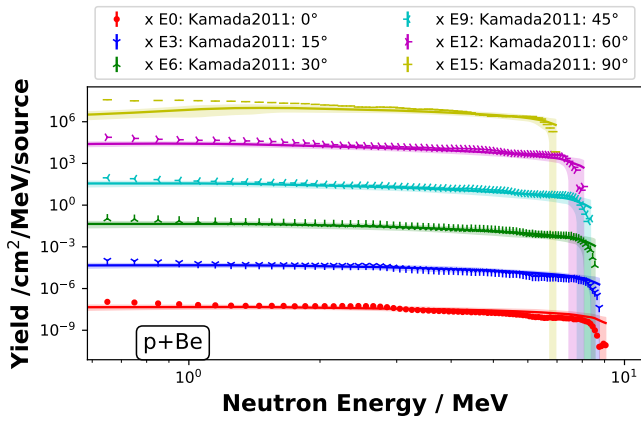
sets are comparable to the model derived here due to different experimental setups, the focus on cross-section measurements with thin targets, and energies of interest larger than 100 MeV.

It is visible that the model, displayed in Figure 7 deviates from the data in the low energy region below 1 MeV. The dataset from Howard et al. taken in 2001 with $E_p = 3 \text{ MeV}$ [17] could not be adequately reproduced and is therefore not displayed here. Both observations have the same reason, for low energy neutrons, the count rates in the Monte Carlo code were too low; as such, the relative uncertainty is as high as 100 %.

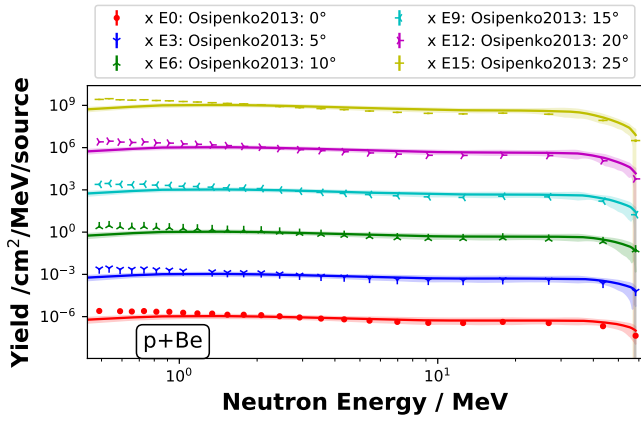
3.3. Spectra for different conventional setups

We can use the model to compare different setups to each other. The variations do differ in the number of particles and the input energies. Expectations are that higher ion energy correlates to a higher neutron count and higher cutoff energy of the spectrum. The number of neutrons is linearly dependent on the incoming particles due to the superposition principle.

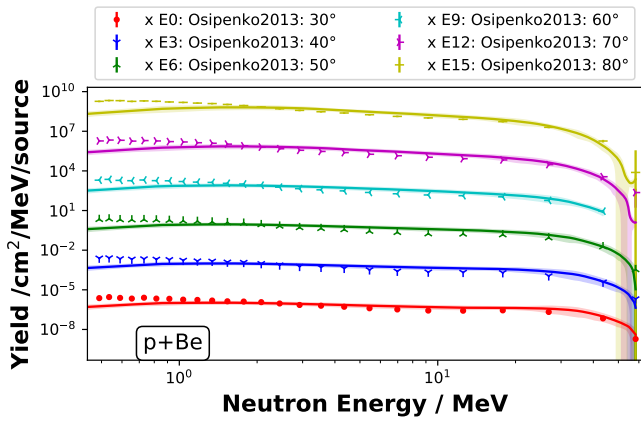
The parameters for the conventional accelerators are extracted from several reports focused on developing compact ion-based neutron sources. Namely the projects HBS in Jülich [2], RANS at RIKEN in Japan [1], SONATE at CEA-Saclay [3], and from the technical report of the IAEA in Vienna [7]. The parameters used for this evaluation are tabulated in Table 3, and the model's results are displayed in 8a and 8b. Differences in the spectrum result from the different particle energies and level differences from the different par-



(a)



(b)



(c)

Figure 7: Experimental data compared to the model (solid lines with shaded uncertainty). (a) Data taken by Kamada et al. in 2011 with $E_p = 11$ MeV [15]. (b) and (c) contain data taken by Osipenko et al. in 2013 with $E_p = 62$ MeV [16]. The scattering angle is listed in the legend, the model prediction is the same color as the data, and the data has been multiplied by a factor as indicated by the legends prefix to increase the readability of the plot.

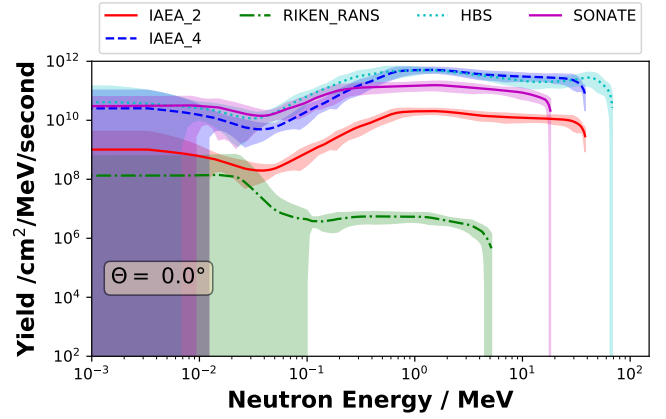
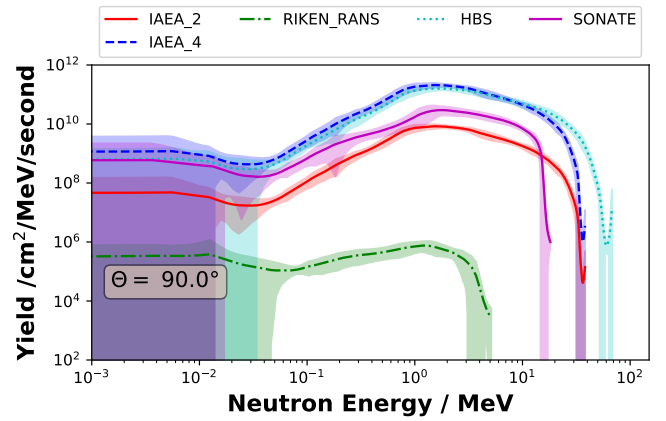
(a) Signal under 0° .(b) Signal under 90° .

Figure 8: Model output for the conventional accelerators in p+Be configuration.

tile counts. The spectral shape also depends on the scattering angle.

3.4. Spectra for Laser Accelerated Protons

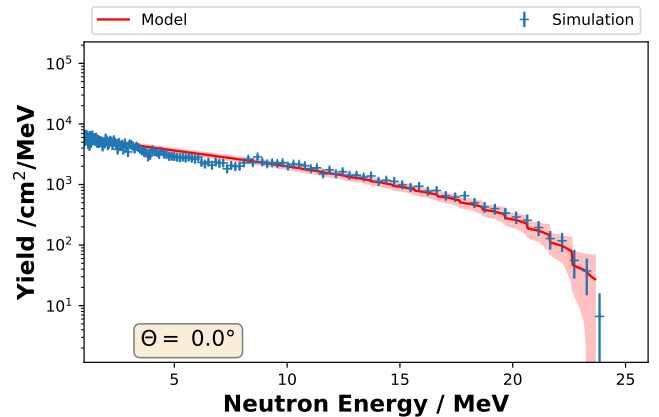
As mentioned previously, the laser-accelerated spectra are calculated by the superposition of several mono-energetic models which follow the composition of the full laser particle spectrum. We tested this on a simulation for the ion spectrum evaluated by Schmitz et al.[18]. The spectrum is analytically given as

$$\frac{dN}{dE}(E) = \frac{N_0}{x} \exp\left(-\frac{x}{k_B T}\right), \quad (5)$$

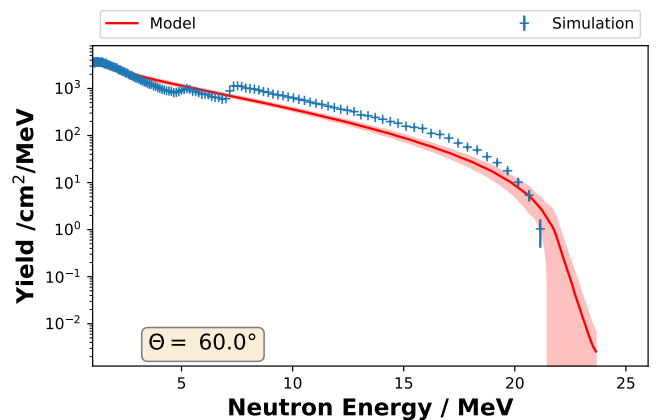
where $N_0 = 3.7 \times 10^{11}$, $k_B T = 7.4$ MeV, and E the spectrum's energy in the interval from 5 MeV to 25.5 MeV. We did additional simulations for this proton spectrum and a corresponding beryllium target with a thickness of 5.02 mm. The results of the simulations, together with the corresponding model output, are displayed in Figure 9. The model output is close to the simulation at 0° . Further deviation towards higher scattering angles causes a larger model deviation from the simulation, indicated by a step in the spectrum at around 7 MeV. This step increases with a larger scattering angle, which indicates a dependency on the underlying geometrical structure of the converter. With a larger angle, the neutron's range inside the converter increases since the transverse dimension of the target is much larger than the thickness of the target in beam direction (240 mm vs. 5.02 mm). This model's smooth behavior is caused by its nature of being a regression model. It smoothes out the spectrum while taking deviations from all angles into account.

4. Conclusion

We presented a predictive surrogate model using an extensive Monte Carlo simulation data set. This model can be deployed quickly and provide the core for quick evaluations of neutron yields, increasing the accessibility of neutron yield simulations and minimizing the need for experience and training for the complex Monte Carlo tools.



(a) Signal under 0° .



(b) Signal under 60° .

Figure 9: Model and simulation output for a TNSA proton beam.

Despite insufficient experimental data for data-driven modeling, our model achieves a good agreement between the model and experimental datasets.

Due to our simulation setup and its numerical feasibility, neutrons from projectile energies $E_p < 5$ MeV have a large uncertainty if $E_n < 1$ MeV. We recommend not trusting the model in this region. The uncertainty, which we calculate by the already explained bootstrapping method in subsection 2.3 is a good indicator of the model’s validity.

The next step to improve this model is to investigate the geometry dependency closer and to increase the cut-off modeling for the neutron spectra. Both could be achieved by new experimental data or an extension of the simulation model.

Author Declarations

The authors have no conflicts of interest to disclose.

Data availability statement

Codes¹ and data² are available in public repositories.

Funding Statement

This work was funded by HMWK through the LOEWE center “Nuclear Photonics.”

This work is also supported by the Graduate School CE within the Centre for Computational Engineering at Technische Universität Darmstadt.

Acknowledgments

We thank Moritz von Treskow and Dimitrios Loukrezis for the helpful discussions on the data pipeline setup and their thoughts on uncertainty quantification for Artificial Neural Networks.

¹<https://git.rwth-aachen.de/surrogat-models/surrogate-modeling-for-neutron-production>

²<https://git.rwth-aachen.de/surrogat-models/neutron-data>

Table A.4: Data for detectors implemented in the Monte Carlo model. Every second value is grayed to guide the eye.

	Θ_{\min}	Θ_{\max}	Θ_{mean}	$\sigma\Theta$	Area cm ²	Ratio %
D01	0	5	0.0	5.0	14.94	0.19
D02	5	10	7.5	2.5	44.72	0.57
D03	10	15	12.5	2.5	74.15	0.94
D04	15	25	20.0	5.0	234.12	2.98
D05	25	35	30.0	5.0	342.26	4.36
D06	35	45	40.0	5.0	440.00	5.60
D07	45	55	50.0	5.0	524.37	6.68
D08	55	65	60.0	5.0	592.81	7.55
D09	65	75	70.0	5.0	643.24	8.19
D10	75	85	80.0	5.0	674.12	8.58
D11	85	95	90.0	5.0	684.52	8.72
D12	95	105	100.0	5.0	674.12	8.58
D13	105	115	110.0	5.0	643.24	8.19
D14	115	125	120.0	5.0	592.81	7.55
D15	125	135	130.0	5.0	524.37	6.68
D16	135	145	140.0	5.0	440.00	5.60
D17	145	155	150.0	5.0	342.26	4.36
D18	155	165	160.0	5.0	234.12	2.98
D19	165	170	167.5	2.5	74.15	0.94
D20	170	175	172.5	2.5	44.72	0.57
D21	175	180	180.0	5.0	14.94	0.19

Appendix A. Detector Details

The radius of the detector sphere is 25 cm. The area of the detector is the absolute covered area of the specific detector, and the Ratio is the percentage of full coverage. Θ_{\min} and Θ_{\max} values describe the minimum and maximum scattering angle the detector can measure. Θ_{mean} is the central scattering angle of the detector.

Appendix B. Hyperparameters

We used the Rectified Linear Unit (ReLU) for the activation function, which is widely used for Regression problems. The identity is employed for the activation function for the last step to the output layer. Similarly, we chose the mean squared error, suited for regression problems, as loss, and it was minimized using the Adam optimizer with

$\beta_1 = 0.9$, $\beta_2 = 0.999$ and $\epsilon = 1 \times 10^{-7}$. The initial learning rate was 0.001, which was lowered to a minimum of 0.0001 during training should the optimizer detect a plateau in the validation loss value (Keras' ReduceLROnPlateau feature).

Considering the resampling, each simulation output contains information about ~ 500 locations (400 raw data + 100 resampled data) in the energy spectrum. Hence, the available data length for the continuous spectral model was $54\,768 \times 400 = 21\,907\,200$ data points. Of these, we used 81% for training, 9% Every training used a batch size of 16 and an early stopping mechanism. Each hidden layer in the network has an L1 regularization strength of 3.56×10^{-7} and an L2 regularization strength of 1×10^{-14} . Since the maximum energy is only predicted per simulation and not per energy bin of the energy spectra, the model for the cut-off energy was trained on 54 768 unique data points. This significantly smaller dataset made the model training faster. The L1 regularization strength was set to 6.2613×10^{-7} , and the L2 regularization strength was set to 2.0392×10^{-8} .

References

- [1] Y. Otake, Riken compact neutron systems with fast and slow neutrons, *Plasma and Fusion Research* 13 (2018) 2401017–2401017. doi:10.1585/pfr.13.2401017.
- [2] U. Rucker, T. Cronert, J. Voigt, J. P. Dabruck, P. E. Doege, J. Ulrich, R. Nabbi, Y. Beßler, M. Butzek, M. Büscher, C. Lange, M. Klaus, T. Gutberlet, T. Brückel, The jülich high-brilliance neutron source project, *The European Physical Journal Plus* 131 (1) (1 2016). doi:10.1140/epjp/i2016-16019-5.
- [3] Thulliez, Loïc, Letourneau, Alain, Schwindling, Jérôme, Chauvin, Nicolas, Sellami, Nadia, Ott, Frédéric, Menelle, Alain, Annighöfer, Burkhard, First steps toward the development of sonate, a compact accelerator driven neutron source, *EPJ Web Conf.* 239 (2020) 17011. doi:10.1051/epjconf/202023917011.
- [4] ESFRI Physical Sciences and Engineering Strategy Working Group - NeutronLandscape Group, Neutron scattering facilities in Europe - Present status and future perspectives, Vol. 1, *European Strategy Forum on Research Infrastructures*, 2015.
URL https://www.esfri.eu/sites/default/files/NGL_CombinedReport_230816_Completedocument_0209-1.pdf
- [5] H. Conrad, *Handbook of Particle Detection and Imaging*, Springer International Publishing, 2021, Ch. Spallation: Neutrons Beyond Nuclear Fission, pp. 1001–1040. doi:10.1007/978-3-319-93785-4_30.
URL https://doi.org/10.1007/978-3-319-93785-4_3
- [6] M. Roth, M. Schollmeier, Ion acceleration—target normal sheath acceleration, *CERN Yellow Reports (2016) Vol 1 (2016): Proceedings of the 2014 CAS–CERN Accelerator School: Plasma Wake Acceleration* doi:10.5170/CERN-2016-001.231.
- [7] International Atomic Energy Agency, *Compact Accelerator Based Neutron Sources*, no. 1981 in *TECDOC Series*, INTERNATIONAL ATOMIC ENERGY AGENCY, Vienna, 2021.
URL <https://www.iaea.org/publications/14948/compact-accelerator-based-neutron-sources>
- [8] A. Buefler, Contraband detection with fast neutrons, *Radiation Physics and Chemistry* 71 (3-4) (2004) 853–861. doi:10.1016/j.radphyschem.2004.04.110.
- [9] T. Sato, Y. Iwamoto, S. Hashimoto, T. Ogawa, T. Furuta, S. ichiro Abe, T. Kai, P.-E. Tsai, N. Matsuda, H. Iwase, N. Shigyo, L. Sihver, K. Niita, Features of particle and heavy ion transport code system (PHITS) version 3.02, *Journal of Nuclear Science and Technology* 55 (6) (2018) 684–690. doi:10.1080/00223131.2017.1419890.
- [10] R. Forrest, R. Capote, N. Otsuka, T. Kawano, A. Koning, S. Kunieda, J.-C. Sublet, Y. Watanabe, Fendl-3 library summary documentation, Tech. rep., International Atomic Energy Agency, Vienna, Austria (12 2012).
URL <https://nds.iaea.org/publications/indc/indc-nds-0628/>
- [11] P. Diaconis, B. Efron, Computer-intensive methods in statistics, *Scientific American* 248 (5) (1983) 116–130. doi:10.1038/scientificamerican0583-116.
- [12] B. Efron, C. Stein, The jackknife estimate of variance, *The Annals of Statistics* 9 (3) (may 1981). doi:10.1214/aos/1176345462.
- [13] N. Otuka, E. Dupont, V. Semkova, B. Pritychenko, A. Blokhin, M. Aikawa, S. Babykina, M. Bossant, G. Chen, S. Dunaeva, R. Forrest, T. Fukahori, N. Furutachi, S. Ganesan, Z. Ge, O. Gritzay, M. Herman, S. Hlavač, K. Katō, B. Lalremruata, Y. Lee, A. Makinaga, K. Matsumoto, M. Mikhaylyukova, G. Pikulina, V. Pronyaev, A. Saxena, O. Schwerner, S. Simakov, N. Soppera, R. Suzuki, S. Takács, X. Tao, S. Taova, F. Tárkányi, V. Varlamov, J. Wang, S. Yang, V. Zerkin, Y. Zhuang, Towards a more complete and accurate experimental nuclear reaction data library (exfor): International collaboration between nuclear reaction data centres (nrdc), *Nuclear Data*

- Sheets 120 (2014) 272–276. doi:<https://doi.org/10.1016/j.nds.2014.07.065>.
URL <https://www.sciencedirect.com/science/article/pii/S0090375214005171>
- [14] V. Zerkin, B. Pritychenko, The experimental nuclear reaction data (exfor): Extended computer database and web retrieval system, Nuclear Instruments and Methods in Physics Research Section A: Accelerators, Spectrometers, Detectors and Associated Equipment 888 (2018) 31–43. doi:<https://doi.org/10.1016/j.nima.2018.01.045>.
URL <https://www.sciencedirect.com/science/article/pii/S0168900218300627>
- [15] S. Kamada, T. Itoga, Y. Unno, W. Takahashi, T. Oishi, M. Baba, Measurement of energy-angular neutron distribution for ${}^7\text{Li}$, ${}^9\text{Be}(p,xn)$ reaction at $E_p = 70$ mev and 11 mev, Journal of the Korean Physical Society 59 (2) (2011) 1676. doi:[10.3938/jkps.59.1676](https://doi.org/10.3938/jkps.59.1676).
URL <http://dx.doi.org/10.3938/jkps.59.1676>
- [16] M. Osipenko, M. Ripani, R. Alba, G. Ricco, M. Schillaci, M. Barbagallo, P. Boccaccio, A. Cellentano, N. Colonna, L. Cosentino, A. Del Zoppo, A. Di Pietro, J. Esposito, P. Figuera, P. Finocchiaro, A. Kostyukov, C. Maiolino, D. Santonocito, V. Scuderi, C. Viberti, Measurement of neutron yield by 62mev proton beam on a thick beryllium target, Nuclear Instruments and Methods in Physics Research Section A: Accelerators, Spectrometers, Detectors and Associated Equipment 723 (2013) 8–18. doi:<https://doi.org/10.1016/j.nima.2013.04.074>.
URL <https://www.sciencedirect.com/science/article/pii/S0168900213005081>
- [17] W. B. Howard, S. M. Grimes, T. N. Massey, S. I. Al-Quraishi, D. K. Jacobs, C. E. Brient, J. C. Yanch, Measurement of the thick-target ${}^9\text{Be}(p,n)$ neutron energy spectra, Nuclear Science and Engineering 138 (2001) 145. doi:[10.13182/NSE01-A2206](https://doi.org/10.13182/NSE01-A2206).
URL <http://dx.doi.org/10.13182/NSE01-A2206>
- [18] B. Schmitz, M. Metternich, O. Boine-Frankenheim, Automated reconstruction of the initial distribution of laser accelerated ion beams from radiochromic film (RCF) stacks, Review of Scientific Instruments 93 (9) (2022) 093306. doi:[10.1063/5.0094105](https://doi.org/10.1063/5.0094105).